


Study of Unsteady Surface Flowfields on and Around Turrets with Different Protrusions

Timothy J. Bukowski* and Stanislav Gordeyev†
University of Notre Dame, Notre Dame, Indiana 46556

Matthew Kalensky‡
U.S. Naval Surface Warfare Center, Dahlgren, Virginia 22448
and

Matthew R. Kemnetz§
U.S. Air Force Research Laboratory, Kirtland Air Force Base, New Mexico 87117

<https://doi.org/10.2514/1.J062971>

Wind-tunnel experiments were conducted to measure the unsteady surface pressure field on and around a hemisphere-on-cylinder turret of varying protrusion in subsonic flow. These measurements were obtained using fast-response pressure-sensitive paint coupled with pressure transducers. The surface pressure field data resulting from Mach 0.5 flow ($Re_D \approx 2 \times 10^6$) over a partially submerged hemisphere, a hemisphere, and a hemisphere on a cylinder were analyzed using proper orthogonal decomposition modal analysis, as well as a variant of this approach referred to as joint proper orthogonal decomposition. The results showed that decreased turret protrusion into the freestream flow reduced the prevalence of antisymmetric surface pressure field fluctuations caused by antisymmetrical vortex shedding. The frequency associated with this fluctuation was found to be around $St_D \approx 0.19$. When a partial hemispherical turret geometry was used, it was shown that the antisymmetric mode was greatly suppressed; and the wake was dominated by a symmetric mode with a broadband spectral peak at a higher frequency of $St_D \approx 0.3$. This suggests that there is a “mode switching” as the protrusion is changed from the hemisphere to the partial hemisphere configuration. An optical flow approach was used to find the convective velocity field in the wake, from which topological flow features could be identified. The size of the wake separation region was found to grow smaller with the decreased protrusion while keeping a similar shape.

Nomenclature

A, B	=	calibration coefficients
a	=	proper orthogonal decomposition mode temporal coefficient
b	=	joint proper orthogonal decomposition mode temporal coefficient
C_p	=	pressure coefficient
D	=	turret diameter
F	=	free variable
f	=	frequency
I	=	image pixel intensity
M	=	Mach number
p	=	static pressure
R	=	turret radius
R_{base}	=	radius of turret where it meets the wind-tunnel wall
R_p	=	two-point cross-correlation matrix
Re_D	=	Reynolds number based on turret diameter
St_D	=	Strouhal number based on turret diameter
s	=	spatial vector
t	=	temporal vector
U	=	x -direction velocity component
V	=	z -direction velocity component

w	=	wake separation region width
x, y, z	=	flow coordinates
ϵ	=	constant
λ	=	proper orthogonal decomposition mode eigenvalue
ϕ	=	proper orthogonal decomposition mode
ψ	=	joint proper orthogonal decomposition mode

Subscripts

n	=	proper orthogonal decomposition and joint proper orthogonal decomposition mode number
ref	=	reference
rms	=	root mean square
v	=	wake vortex location
∞	=	freestream value

1. Introduction

THERE has been considerable research regarding the integration of laser propagation systems onto airborne vehicles [1–3]. For this application, hemispherical turret beam director geometries have been of high interest due to their simple design and wide field of regard. However, the protrusion of this nonaerodynamic shape out of the aircraft creates a complicated three-dimensional turbulent flowfield. This flowfield results in an unsteady pressure field that 1) leads to an unsteady density field causing aero-optic beam aberrations and 2) causes unsteady forcing on the turret, leading to a complicated fluid–structure interaction, both of which degrade the performance of an aircraft-mounted laser propagation system. Although the aero-optic environment caused by turrets has been studied in depth [1,4–7], understanding the forcing imposed onto the turret is a newer field of study. Keeping the application of aircraft-mounted laser propagation systems in mind, unsteady forcing on the turret can result in the vibration of optical-path components inside the turret. These vibrations may cause optical-path components such as mirrors to rotate, which in turn imposes angular distortions onto the outgoing laser beam, resulting in a net unsteady deflection of the beam from a desired aim point at the target plane [8,9]. For many beam control

Received 6 March 2023; revision received 11 July 2023; accepted for publication 18 July 2023; published online 14 August 2023. Copyright © 2023 by the authors. Published by the American Institute of Aeronautics and Astronautics, Inc., with permission. All requests for copying and permission to reprint should be submitted to CCC at www.copyright.com; employ the eISSN 1533-385X to initiate your request. See also AIAA Rights and Permissions www.aiaa.org/randp.

*Graduate Research Assistant, Department of Aerospace and Mechanical Engineering; tbukowski@nd.edu. Student Member AIAA.

†Associate Professor, Department of Aerospace and Mechanical Engineering. Associate Fellow AIAA.

‡Engineer, Integrated Engagement Systems Department, Dahlgren Division. Member AIAA.

§Research Aerospace Engineer, Directed Energy Directorate. Member AIAA.

applications, it is desirable to minimize this “beam jitter”: to do so, the unsteady forcing on the turret needs to be better understood. The work presented in this paper explores the unsteady pressure fields that create this forcing environment for different turret geometries.

It is beneficial for the discussion in this paper to briefly discuss the known fluid mechanics associated with flow over a hemispherical turret. Incoming subsonic flow stagnates at the lower-frontal portion of the turret and creates a coherent vortical structure that extends around the turret and then convects downstream. This structure is referred to as the “necklace” vortex. The fluid incident on the upper-frontal part of the turret stagnates and then accelerates over the top of the hemispherical body. The frontal region of the turret is fairly steady. The fluid that convects over the top of the turret eventually separates due to the adverse pressure gradient. For Reynolds numbers greater than $\approx 3 \times 10^5$, separation typically occurs around 120 deg relative to the incoming freestream. Once the flow separates, a shear layer forms between the freestream flow over the turret and the separation region directly downstream of the turret body. Symmetrical counter-rotating vortices, referred to as “horn” vortices, form in the wake region. At low Mach numbers, the turbulent structures in this wake are more coherent. As the Mach number increases, the horn vortices lose their symmetry; and additional vortices begin shedding off the back of the turret. The fluid mechanics are summarized in depth in a review found in Ref. [1]. These structures can be seen in the schematic shown in Fig. 1.

Recent work has begun to investigate the surface pressure field characteristics of a turret in subsonic flow. In Ref. [10], wind-tunnel tests were conducted to investigate the unsteady pressure fields around a turret, with an emphasis on exploring the effects of realistic surface features. This work was foundational for a few reasons. It was the first set of experiments to use pressure-sensitive paint (PSP) for the application of investigating the surface pressure field of an optical turret. The high resolution of PSP has made it a powerful diagnostic tool, alleviating the issue of having a spatially sparse array of measurements when using fast-response pressure transducers. In addition, the temporal resolution of PSP has increased significantly in the last few years, with polymer-ceramic pressure-sensitive paint (PC-PSP) having a temporal response as low as $35 \mu\text{s}$ [11].

Thus, PSP has become a valuable diagnostic tool for investigating the unsteady surface pressure field on and around optical turrets in subsonic and transonic flows, and it has made data reduction techniques such as proper orthogonal decomposition (POD) and optical flow viable. With access to the full three-dimensional surface pressure fields of the optical turret afforded by the use of PSP, Ref. [10] was also the first to heavily rely on POD to analyze the data for this application. As was shown, valuable physical flow insight can be gleaned from modal analysis data reduction techniques. Motivated by the results and experiments of Ref. [10], additional experiments were conducted to specifically investigate the wake dynamics downstream of the turret at subsonic and transonic speeds in Refs. [12,13]. Here, POD helped reveal two important behaviors: a cross-stream antisymmetric shifting mode, and a cross-stream symmetric breathing mode. In Ref. [14], it was shown that the antisymmetric shifting mode accounted for nearly 100% of the cross-stream z -component forcing

on the turret, whereas the symmetric breathing mode only forced the turret in the streamwise x -component and wall-normal y -component directions. To address possible aeroelastic effects on the turret wake, Roeder and Gordyev [15] conducted experiments designed to study the fluid–structure interaction of a turret in subsonic flow. These tests, coupled with POD and optical flow analysis, revealed that when the turret is mounted such that it can oscillate due to the unsteady forcing imposed by the flow, the resulting changes in the wake are relatively small, even for oscillations of rather large amplitude (on the order of 1 mm or 0.2% of the turret radius). Recognizing that the turret motion in realistic systems is typically less than that, these experiments suggested that the aeroelastic effects can be ignored while studying the wake dynamics and the related unsteady forcing acting on the turret. In lower-Reynolds-number studies ($Re < 3 \times 10^5$), it has been observed that a large boundary with a thickness larger than the hemisphere does not have any significant effects on dynamics [16]. Savory and Toy conducted a parametric study to investigate the effects of the boundary layer, the surface roughness, and the Reynolds number on flow over a hemisphere [17]. For a hemisphere undergoing laminar separation, the surface roughness was shown to effectively increase the Reynolds number, leading the boundary layer to transition to turbulent at lower actual Reynolds numbers and, as a result, delay separation. However, for hemispheres that already exhibit turbulent separation, higher roughness causes separation to occur further upstream. It was shown that a thicker boundary layer decreases the size of the recirculation region behind a hemisphere. It was also shown that a larger boundary layer grows the necklace vortex, which contributes to vorticity in the far wake. Reference [18] found similar results for flow over a partially submerged hemisphere.

Although the flows around hemispheres on cylinders and hemispheres have been studied in depth, less is known about flow around a partially submerged hemisphere. A computational study of hemisphere and submerged hemisphere turrets with a flat window in Ref. [19] found the variation in cross-stream forcing on the turret to be lower for the submerged turret in subsonic flow. The flowfield and the aero-optical environment around a hemisphere and a submerged hemisphere were studied computationally in Ref. [20], which found that the submerged hemisphere exhibited the same general flow features typical for hemispherical turrets and had lower wave-front distortion than that of the hemisphere. Reference [21] performed flow visualization of the flow over a submerged hemisphere showing similar flow features as for flow over a hemisphere. Experimental wind-tunnel and flight testing performed by Refs. [22–24] quantified aeromechanical jitter of turrets varying in protrusion from a hemisphere-on-cylinder turret down to a submerged hemisphere, but no discernible scaling was found. However, through POD analysis of the pressure field, they did find that there was a significant change in flow behavior from a predominantly antisymmetric flow to predominantly symmetric flow when the protrusion changed from a hemisphere to a submerged hemisphere. Malkus et al. [25] found a clear antisymmetric shifting mode and a symmetric breathing mode through computational work done at $M = 0.8$, and they found that this mode switching likely occurs when the hemisphere is around 80% exposed. Based on these previous studies, it has been hypothesized that reducing the protrusion of the turret into the flow may reduce the fluid-induced forcing on the optical turret, especially in the cross-stream direction. For the application of laser propagation systems, reduced forcing by the flowfield may reduce system beam jitter.

In this paper, wind-tunnel experiments were conducted to investigate the unsteady surface pressure field on a hemisphere-on-cylinder turret as a function of protrusion distance. This was achieved by collecting simultaneous fast-response PSP imagery coupled with surface-mounted pressure transducers. The experiments conducted to obtain these data are described in depth in Sec. II. The data reduction steps required to convert measured image intensity to meaningful surface pressure field data are described in Sec. III. Furthermore, optical flow, POD, and a variant of POD referred to as joint proper orthogonal decomposition (JPOD) were used to analyze the surface pressure field obtained from the PSP imagery. Each of these data reduction tools is also summarized in Sec. III. In

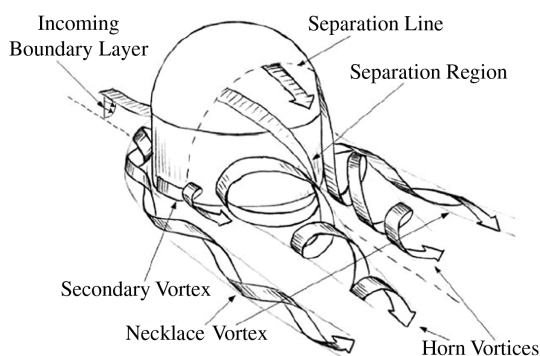


Fig. 1 Schematic of major flow structures for flow around a hemisphere-on-cylinder turret [1].

Sec. IV, the data processing tools introduced in Sec. III are employed to relate the surface pressure characteristics to the turbulent flowfield. Specifically, convective velocity fields calculated using optical flow were used to characterize the wake. POD was used to further understand the prominent structures in the flow over the turret and in the wake. Finally, JPOD was then used to compare unsteady pressure fields between different geometries. A summary and conclusions are given in Sec. V.

II. Experimental Setup

The surface pressure was measured for flow over and around a hemisphere-on-cylinder turret with varying protrusion in Mach 0.5 subsonic flow. A shell of the Airborne Aero-Optics Laboratory (AAOL) turret was used, which has produced many foundational datasets and impactful results [26–29] in the aero-optics community. This hemisphere-on-cylinder turret has a radius of $r = 0.15$ m (6 in.). It is worth noting that the AAOL turret model is not a smooth hemisphere-on-cylinder turret but rather has realistic surface features, such as small gaps between the stationary turret shell and the rotating “donut” part, screw holes, etc. An image of this turret configured in the wind tunnel is shown in Fig. 2. The turret protruded from the wall at different heights of 0.07 m (2.75 in.), 0.15 m (6 in.), 0.19 m (7.5 in.), and 0.27 m (10.5 in.). The lowest protrusion geometry of 0.07 m is referred to as the “partial hemisphere,” which protrudes about 45% of the hemisphere radius. The 0.15 m protrusion configuration is referred to as the “hemisphere” case, and the 0.19 m protrusion configuration is referred to as the “hemisphere + cylinder” case. These different protrusion cases were tested in the University of Notre Dame’s White Field Mach 0.6 wind tunnel. This wind tunnel has a 0.91×0.91 m (3×3 ft) test section, and data were collected at a freestream Mach number of 0.5 ($Re_D \approx 2 \times 10^6$, $U_\infty \approx 170$ m/s). This facility is particularly useful because the dynamic pressures

are similar to those seen in flight. The incoming boundary layer was not measured for these tests; however, previous tunnel characterization has shown the boundary-layer thickness to be on the order of 25 mm (1 in.) and the turbulence intensity to be below 1% [30]. This boundary layer thickness is relatively thin compared to the turret height for all cases with the relative boundary layer thickness being 36%, 16%, and 9% of the height of the partial hemisphere, hemisphere, and hemisphere + cylinder, respectively.

The tunnel blockages were about 5.1% for the hemisphere + cylinder, 4.4% for the hemisphere, and 1.9% for the partial hemisphere. However, the cross-stream blockage, which measures the ratio of turret diameter at the wall to the width of the test section, was higher at 33% for the hemisphere + cylinder and hemisphere cases and 28% for the partial hemisphere case. This cross-stream blockage limits the available space along the sides of the tunnel, hindering the formation of the wake and flow structures. This interference with the natural flow dynamics is a result of insufficient room for unimpeded development of the flow near the walls. Comparison between the tunnel tests at the same tunnel and flight tests, where there was no blockage, indicated that the separation line on top of the hemisphere + cylinder turret might be delayed by as much as 6 deg [31]. Therefore, the findings presented here should be considered preliminary, and further investigations into the impact of cross-stream blockage on wake dynamics are planned for the future.

A fast-response PC-PSP [11,32,33] was used to measure the surface pressure on the surface of the turret as well as on a 0.3×0.61 m (12×24 in.) wake plate in the downstream portion of the turret geometry. The PSP was approximately $100 \mu\text{m}$ thick and was excited by eight UV-light sources: four of which are visible in Fig. 2 (left). Also shown in the left plot of Fig. 2 is the painted wake plate and turret for the hemisphere + cylinder geometry. The resulting luminescence was measured by two synchronized high-speed Phantom cameras (v1611 and v2512), with one on each side of the wind-tunnel

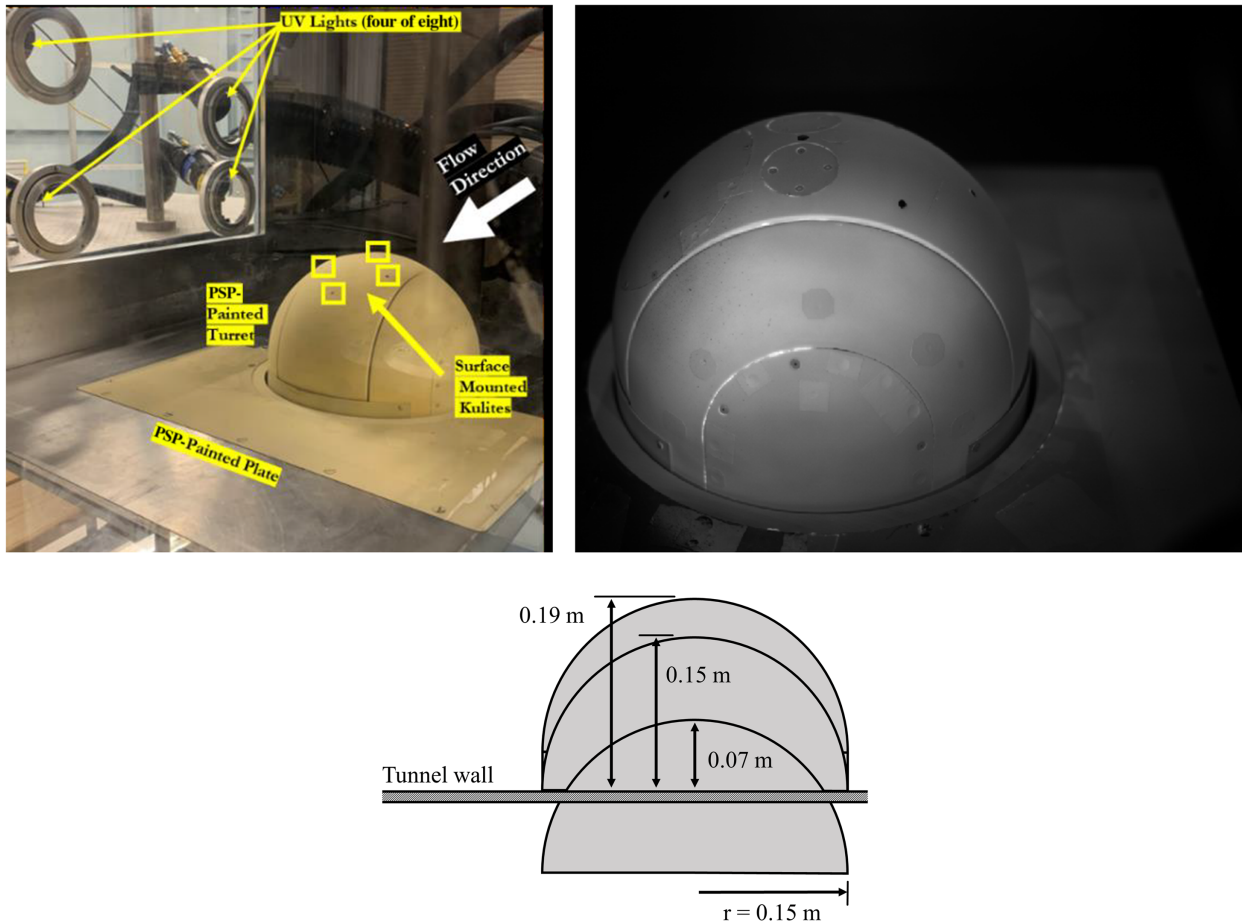


Fig. 2 Hemisphere + cylinder turret setup inside the wind tunnel (top left). Beige regions are where PSP was applied. Sample image from PSP video for hemisphere + cylinder turret (top right). Diagram of different configurations tested (bottom).

test section. Both cameras collected imagery at a frame rate of 3 kHz. Four Kulite XT-140 unsteady pressure transducers were installed flush to the surface of the turret, as shown in Fig. 2 (left), which allowed for the in situ calibration of the PSP. Data collection of the pressure transducers was synchronized with the cameras and recorded unsteady pressures for 5.33 s at a sample rate of 30 kHz. The tunnel temperature, static pressure, and laboratory atmospheric pressure were recorded before and after the tests.

III. Data Reduction

A. Surface Pressure Reconstruction

The general process for surface pressure reconstruction and PSP calibration was similar to that used in Refs. [10,23]. The two-dimensional images from both cameras were used to reconstruct the pressure field of a three-dimensional surface. This conversion was accomplished using a perspective transformation matrix (PTM) [34–36]. Here, images of the features within the field of view at known locations in three-dimensional space were collected with both cameras. The PTM was constructed using these images to map pixels to a physical location. A mesh over the areas of interest was created and mapped onto the images collected from both cameras. The mesh in the wake region was rectangular with grid steps of 7.6 mm (0.3 in.), whereas the dome had a spherical mesh with grid steps of 3 deg in both the azimuthal and elevation directions. Mesh points were not included at the locations of the unsteady pressure sensors because the wall-mounted sensors themselves were not painted. For the hemisphere and hemisphere + cylinder cases, small semicircular regions at the front and the aft portions of the turret were also excluded from the turret mesh. These regions were imaged at severely oblique angles (greater than 80 deg), where PSP has a poor response. Mesh points were also not included in the region where the turret body meets the tunnel wall because the transition could not be clearly defined in the images. The mesh from the perspective of one of the cameras is presented in Fig. 3 for each of the three turret geometries.

To convert pixel intensities to pressure, the intensities for pixels closest to the mesh locations were extracted and spatially filtered by taking the average of the pixels forming an 11×11 square centered on the pixel of interest. The intensity values I recorded by the cameras were converted to static pressure P through the Stern–Volmer equation,

$$\frac{I_{\text{ref}}(s)}{I(s, t)} = A + B \frac{p(s, t)}{p_{\text{ref}}} \quad (1)$$

where P_{ref} was the ambient laboratory pressure, and I_{ref} was the temporal mean of the reference data taken with the wind-tunnel flow off and the UV lights on. Variables A and B are calibration constants calculated for each camera and geometry in situ. Specifically, these constants were calculated using the temporal mean pressure from the unsteady pressure sensors and intensity values from pixels surrounding the pressure sensor in the image data. The calibration curves for these data are presented in Ref. [23]. The calibration coefficients in Eq. (1) also depend on the temperature variations [33], potentially affecting the accuracy of the pressure measurements. The temperature was measured before and after each run and was found to increase by less than 2°C. Temperature effects on the calibration coefficients were ignored. However, after data were converted to pressure, a line was fit to the data; and temperature drift effects were

accounted for by removing this line instead of the mean from the data when calculating flow fluctuations.

After data from the two cameras were converted to spatial pressure fields at the defined mesh locations, data from both cameras were blended together using spatial weighting functions. This allowed for a single data matrix to represent the full surface pressure field of the turret, similar to what was done in Ref. [10].

B. Convective Surface Velocity

The mean surface convective velocity field was found for the wake region using the optical flow method. This method assumes the surface pressure field to be primarily a convecting field and solves for velocity from a convective equation for pressure, which is given as

$$\frac{\partial p(x, z, t)}{\partial t} + U(x, z) \frac{\partial p(x, z, t)}{\partial x} + V(x, z) \frac{\partial p(x, z, t)}{\partial z} = 0 \quad (2)$$

where $U(x, z)$ is the convective velocity in the streamwise x direction, and $V(x, z)$ is the convective velocity in the cross-stream z direction. If the pressure field is given at several consecutive time points, Eq. (2) can be treated as an overdetermined system of equations for the two velocity components at each spatial point. This system was then solved using least-squares minimization as proposed in Refs. [37–39]. This method was also used in Ref. [15] to calculate surface velocity fields from surface pressure fields for flow around a hemisphere. In the work presented here, an additional term, $\epsilon F(x, z)$, was added to Eq. (2) as follows:

$$\frac{\partial p(x, z, t)}{\partial t} + U(x, z) \frac{\partial p(x, z, t)}{\partial x} + V(x, z) \frac{\partial p(x, z, t)}{\partial z} + \epsilon F(x, z) = 0 \quad (3)$$

Here, $F(x, y)$ is a free variable and ϵ is a positive constant. Adding this additional term was found to create smoother results as compared to using Eq. (2). Different values of ϵ ranging from 1×10^{-20} to 1×10^{20} were tested, and the results were found to be largely insensitive to the ϵ value. The value of $\epsilon = 1 \times 10^{-5}$ was used in the presented results. All derivatives in Eq. (3) were calculated numerically using the central difference method.

C. Proper Orthogonal Decomposition

POD was used to analyze the dynamics of the unsteady pressure field on the turret and in the wake region. POD is commonly used as a means for creating a low-order reconstruction of spatiotemporal data, where data can be represented using a reduced number of spatial modes [40]. In POD, the globally reconstructed spatiotemporal fluctuating pressure field $p(s, t)$, where $s = (x, y, z)$ denotes a spatial point, is decomposed into a series of spatial POD modes $\phi_n(s)$ and corresponding temporal coefficients $a_n(t)$, such as

$$p(s, t) = \sum_n a_n(t) \phi_n(s)$$

The POD modes are the solutions to the eigenvalue problem

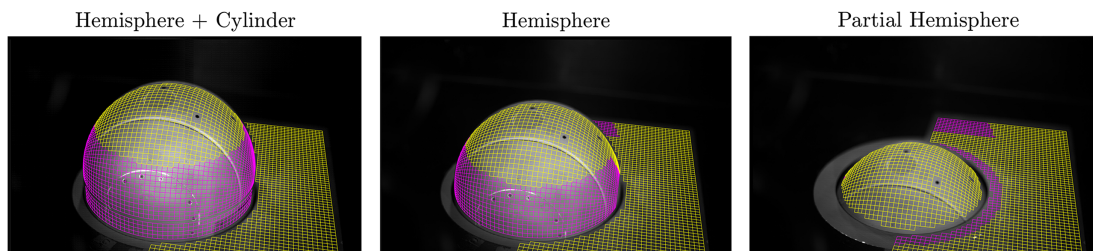


Fig. 3 Mesh used, which has been overlaid on top of an example image. The region in yellow is the common region for all turret geometries used for JPOD analysis. The purple and yellow regions together were used for POD. Flow goes from left to right.

$$\int_{s'} R_p(s, s') \phi_n(s') ds' = \lambda_n \phi_n(s) \quad (4)$$

where $R_p(s, s') = \overline{p(s, t)p(s', t)}$ is the two-point cross-correlation matrix, and the overbar here and later in this paper denotes the temporal averaging. Using this correlation matrix, we get mode shapes showing regions in the surface pressure field that are correlated and anticorrelated. The energy of each mode is given by the eigenvalue λ_n . By construction, the POD modes are orthonormal, $\int_s \phi_n(s) \phi_m(s) ds = \delta_{nm}$ where δ_{nm} is a Kronecker delta. The temporal coefficients can be found by projecting the pressure field onto the POD mode,

$$a_n(t) = \int_s p(s, t) \phi_n(s) ds \quad (5)$$

The energy of each mode can also be found directly from the temporal coefficients as $\lambda_n = \overline{a_n^2(t)}$. The cross-correlation function can be recomposed using POD modes as

$$R_p(s, s') = \sum_n \lambda_n \phi_n(s) \phi_n(s') \quad (6)$$

From this relationship, we know the contribution of each POD mode to the overall correlation in the pressure field, where dominant modes have the largest energies. Equations (4) and (5) were discretized using the mesh described in Sec. III, shown as the purple and yellow meshes in Fig. 3. Because the mesh was nonuniform, a weighted version of POD was implemented [40,41]. The MATLAB *eig* function was used to solve Eq. (4) and decompose the surface pressure PSP data into individual POD modes and their coefficients.

D. Joint Proper Orthogonal Decomposition

Although an optimal set of modes can be obtained for each dataset using POD, the meshes and modes are different for each case, and so comparing POD modes and related energies for different turret geometries becomes complicated. As an alternative method, JPOD was proposed and used as a data analysis technique to compute the common or joint modes from different datasets [10,15]. JPOD is a specialized version of POD, in which the spatiotemporal data for different cases are combined into a single dataset, and the POD algorithm is used to extract the joint spatial modes. In the present studies, the cross-correlation matrices for all turret configurations were combined to compute a *joint* two-point cross-correlation matrix $R_{p,\text{joint}}(s, s')$,

$$\begin{aligned} R_{p,\text{joint}}(s, s') &= R_p(s, s'; \text{partial hemisphere}) \\ &+ R_p(s, s'; \text{hemisphere}) \\ &+ R_p(s, s'; \text{hemisphere} + \text{cylinder}) \end{aligned} \quad (7)$$

where $R_p(s, s', \text{geometry})$ is the correlation matrix for a given geometry normalized by the square of the spatial mean of the temporal root mean square of its pressure field $\langle p_{\text{rms}}(s) \rangle^2$. The JPOD requires a common mesh, which is shown in yellow in Fig. 3. The JPOD modes $\psi_n(s)$ were computed using $R_{p,\text{joint}}(s, s')$ via Eq. (4). The temporal coefficients of the JPOD modes, denoted as $b(t; \text{geometry})$, were computed by projecting the JPOD modes onto *individual* pressure fields,

$$b_n(t; \text{geometry}) = \int_s p(s, t; \text{geometry}) \psi_n(s) ds \quad (8)$$

From the temporal coefficients, individual energies of the JPOD modes were computed as

$$\Lambda_n(\text{geometry}) = \overline{b_n^2(t; \text{geometry})} \quad (9)$$

By design, this set of spatial JPOD modes is the same for all cases. When the individual datasets for each case are projected onto these

spatial JPOD modes, only the temporal coefficients and the corresponding energies will be different. Thus, the differences among cases will be reflected only in the temporal coefficients and the energy distributions, making it easier to compare the contribution of a specific mode to each geometry.

IV. Results

A. Pressure Fields

The PSP data were used to calculate the surface pressure fields for each of the different turret geometries. Subsequently, the spatial distribution of the temporal root mean square of the coefficient of the fluctuating pressure, $C_{p,\text{rms}}(s) = \sqrt{\overline{C_p^2(s, t)}}$, was calculated (which we will refer to as spatial maps), and the results are shown in Fig. 4. The figures in the top row share the same color axis to compare the fluctuation magnitudes between the geometries. Here, it can be seen that the magnitude of the fluctuations increases with increasing turret protrusion. The figures in the bottom row have varying color axes to emphasize regions of high fluctuation magnitude for a given geometry. For example, we can see the cross-stream extent of the wake was largest for the hemisphere + cylinder case and grew thinner as protrusion decreased. High fluctuation associated with movement of the separation line was clearly visible for the hemisphere and hemisphere + cylinder cases just behind the apex of the turret. However, the separation location was around 90 deg, which was further upstream than what the literature predicts. Flows over a hemisphere and hemisphere + cylinder are expected to separate at approximately 120 deg from the freestream direction (measured from the -x axis) when over the critical Reynolds number of $Re_D > 300,000$. At this point, the boundary layer on top of the turret is turbulent, leading to a delayed separation as compared to subcritical Reynolds numbers where the boundary layer is laminar and separates near 80 deg [1]. For the experiments conducted here, the Reynolds number was well above critical at $Re_D \approx 2 \times 10^6$, and so the boundary layer on the turret should be turbulent. The gaps, screw holes, and other imperfections on the turret surface are likely what led to premature separation. The separation location for experiments discussed here was in a similar location to the separation line observed in Ref. [10], where the same turret was used.

B. Convective Velocity Fields

The optical flow approach introduced in Sec. III.B was used to calculate a mean surface velocity field. Because convecting vortical structures have associated pressure fluctuations, this approach can be used to track the movement of turbulent structures in the flow. It was found that the dome region of the turret lacked coherent, convective flow structures, and so optical flow did not give meaningful results in this region. Thus, only results in the wake region are presented. The results can be seen in Fig. 5, which are plotted as surface streamlines for each of the different turret geometries. Velocity streamlines were calculated from the velocity field using the MATLAB streamline function. In this figure, a few additional topological features are emphasized. The boundary of the separation region, where the streamwise velocity was zero, is marked with a dashed line. The width of the recirculation region, labeled w , was defined as the width of the wake at the furthest upstream measured point, as shown in Fig. 5 (top-left plot). The full length of the recirculation region x_r , ending at the reattachment point and labeled by a white circle, is only visible for the partial hemisphere case. The locations of the vortices (foci) in the recirculation region (x_r, z_r) , which are labeled with red stars in Fig. 5, are also recorded. For the partial hemisphere and the hemisphere cases, the vortices are not fully identifiable, and so the location on the edge of the separated region closest to the turret was used.

By looking at the velocity field for each geometry, we can investigate how the wake topology changes with varying turret protrusion. It should be noted that toward the edge of the wake (around $z/R \approx \pm 0.7$ for the partial hemisphere and $z/R \approx \pm 1.2$ for the hemisphere and hemisphere + cylinder), there were not enough convecting coherent structures, and the optical flow streamlines become random

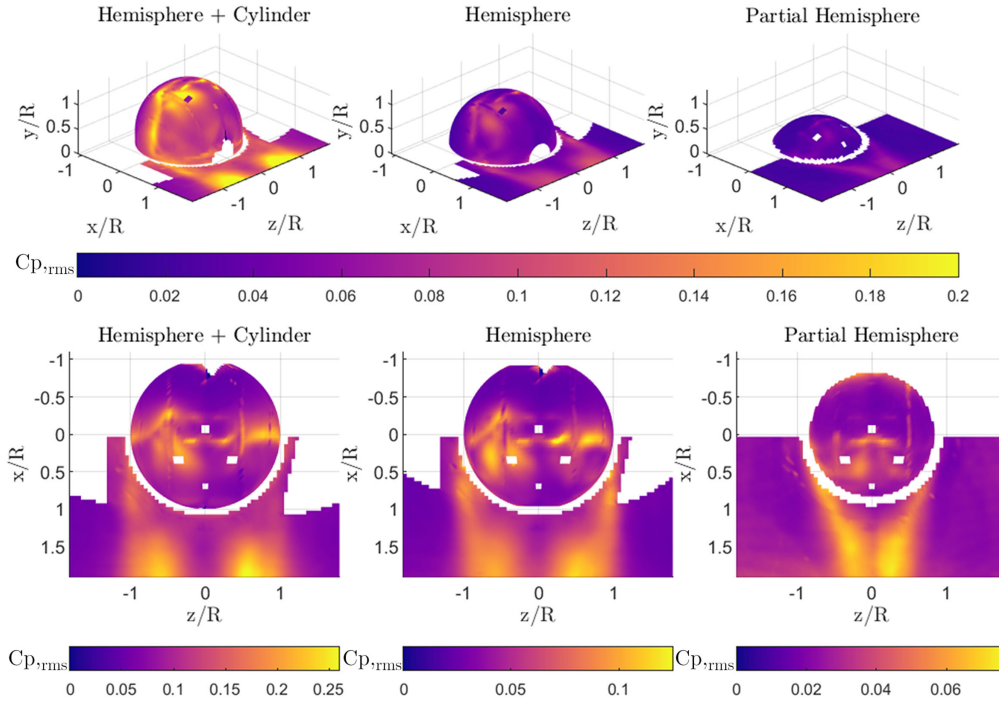


Fig. 4 Spatial maps of pressure fluctuation coefficients $C_{p,rms}$ (s) for each geometry. Flow goes in the positive x direction. Top row has fixed color-map axes. Bottom row has varying color-map values to better visualize the pressure field features.

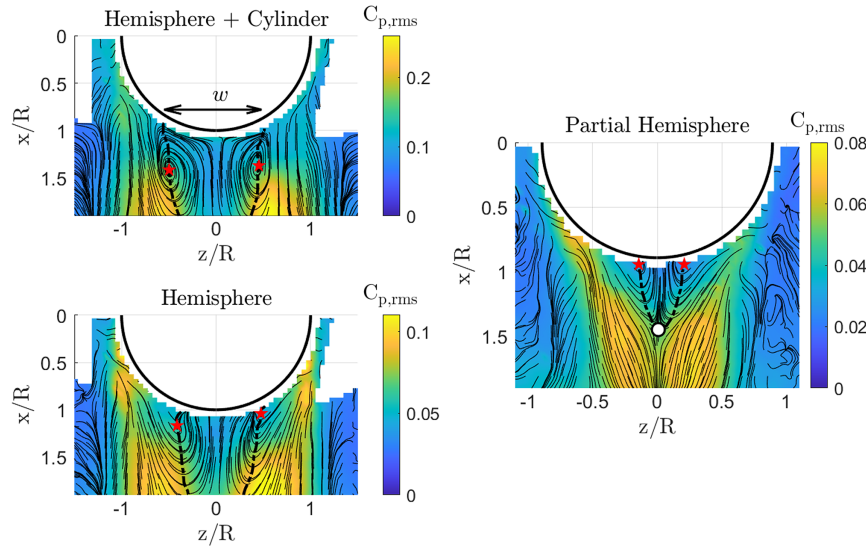


Fig. 5 Streamlines of the velocity field overlaid with pressure fluctuation $C_{p,rms}$. The separation region is outlined by a dashed line. Locations of vortices inside the recirculation region are labeled with red stars, and the reattachment point is labeled with a white circle. The wake width is indicated by w in the top-left plot. Flow goes from top to bottom.

and nonphysical. The separation region widths and the locations of the vortices are summarized in Table 1. The partial hemisphere had the narrowest separation region with a width of $w/R = 0.36$. The separation region grew to $w/R = 0.82$ for the hemisphere case, which is similar to the value of 0.88 found in Ref. [42]. The wake further widened between the hemisphere and the hemisphere + cylinder cases, with $w/R = 1.03$ for the hemisphere + cylinder.

Table 1 Topological features of the recirculation region, defined in Fig. 5, for different turret geometries

	w/R	x_r/R	x_v/R	z_v/R
Hemisphere + cylinder	1.03	—	1.42	0.45
Hemisphere	0.82	—	1.20	0.41
Partial hemisphere	0.36	1.45	0.94	0.16

The shape of the separation region for the partial hemisphere was compared to that of a hemisphere from Ref. [42] by calculating the aspect ratio of the width/length, which is defined as $w/(x_r - R_{base})$. Here, R_{base} is the radius of the turret where it intersects the wall. For the hemisphere case, $R_{base} = R$. We found that for the partial hemisphere case, the separation region had an aspect ratio of 0.66; whereas for the hemisphere in Ref. [42], the aspect ratio was 0.71. These values are fairly similar, with only a slight elongation of the wake as the turret protrusion increases. It has been shown that thick boundary layers can decrease the size of the wake [16,17] due to the increased turbulence intensity. We believe this can be attributed to the lower mean velocity of the flow over top of the turret, resulting in lower momentum, and thus decreasing the length it travels before reattachment. In this experiment, the boundary layer was well below the top of the turret; however, if a turret is toward the back of an aircraft where it is enveloped in the boundary layer, it will likely have a smaller

recirculation region than was measured here. However, in work done on the AAOL, where the turret is only about 4 m from the nose of the aircraft, the boundary layer is around 50 mm (2 in.) [43], which is below the top of the turret; so, we expect the flowfield to be similar to that measured here.

The fluctuating pressure field was overlaid onto the velocity streamlines in Fig. 5 to investigate the relationship between the surface pressure and the velocity field. The recirculation region is associated with the region of relatively low-pressure fluctuation. However, downstream of the reattachment point and outside of the recirculation region, the pressure fluctuations were higher. This increase in the fluctuating pressure was attributed to a combination of unsteady horn vortices shedding around the sides of the turret, as well as the separated flow coming over the top of the turret and impinging on the wall outside the recirculation region.

C. POD Analysis

Before presenting the results of the POD-based analysis, it is important to recognize that POD computes the modes based on the available data. Thus, the modes and the related energies will depend on the region of flow being analyzed. Also, POD imposes the orthogonality restriction on the modes, which may or may not be physical. Thus, one should be careful trying to interpret each POD mode because several of them might be associated with one physical structure. For instance, it is well known that it requires two stationary modes that are shifted in space to represent a traveling structure [40]. Therefore, one way to identify the traveling structure is to look for a pair of spatial modes that are shifted in the convecting direction and have similar spectra and energy contributions.

POD was performed on the fluctuating pressure fields to study prominent spatial features in the flow for different turret geometries. Both the turret and wake regions were analyzed together, allowing us to relate flow features from the two regions. The first four POD modes for each geometry are shown in Fig. 6 along with the modes' associated relative energies. In these plots, yellow (light) and blue (dark) colors represent regions with positive and negative modal values, respectively. As follows from Eq. (6), the cross correlation between two points is proportional to the product of the modes' values

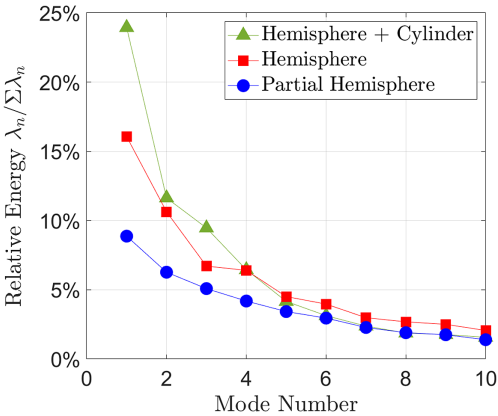


Fig. 7 POD relative modal energy for each geometry.

at these points. Thus, points in the yellow region are anticorrelated with points in the blue region. The relative energies, $\lambda_n / \Sigma \lambda_n$, of the first 10 modes for the three geometries are shown in Fig. 7.

The hemisphere + cylinder and hemisphere geometries have very similar modes, except that the modes for the hemisphere + cylinder case have higher relative energy. Mode 1 contains 24 and 12% of the total energy for the hemisphere + cylinder and hemisphere, respectively. This mode is mostly antisymmetric in the cross-stream direction and represents the shifting mode [44]. The antisymmetric nature of mode 1 is a result of unsteady alternating vortex shedding that has been seen in previous studies [1,10,45]. The pressure fluctuations from the separation line are correlated with fluctuations in the separated region of the wake. Mode 2 for the hemisphere + cylinder and hemisphere geometries, which contains 12 and 11% of the total energy, respectively, is mostly cross-stream symmetric and looks similar to the $C_{p,rms}(s)$ maps in Fig. 4. Mode 2 has a strong cross-stream-symmetric correlation related to the separation line on the top of the dome. This region is rather wide and not quite uniform in the cross-stream direction as compared to the results from Refs. [12,25]. This small asymmetry, also visible in mode 1, is most likely due to the

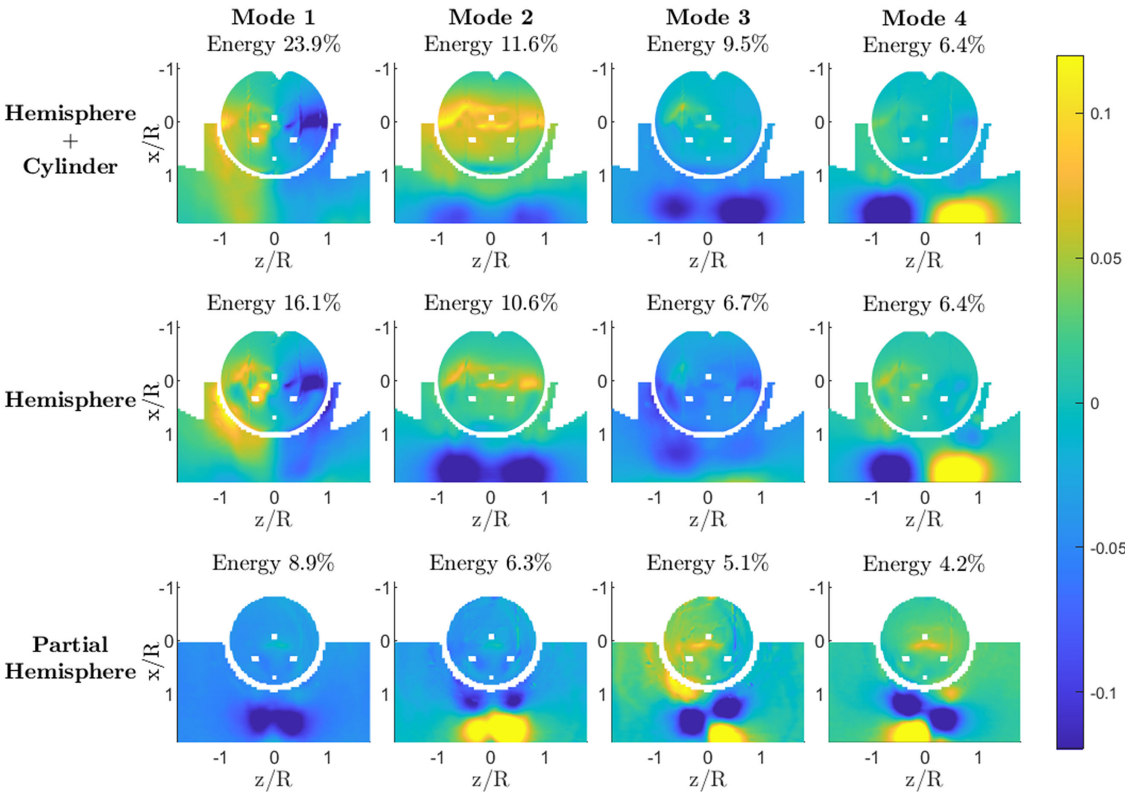


Fig. 6 POD modes for each geometry with associated modal energy. Flow goes from top to bottom.

surface features on the top of the turret dome. Also evident in Fig. 6 is a pair of correlated blue (dark) regions in the wake, which are related to where the flow reattaches. These blue regions are anticorrelated to the region of the separation line on top of the turret. This mode was identified as a wake “breathing” mode, and its dynamics are discussed in Ref. [44]. Mode 3 for the hemisphere and the hemisphere + cylinder geometries is mostly cross-stream symmetric and shows a positive correlation of the wake region. There is a little correlation between the wake region and the separation line on the sides of the turret for the hemisphere, with almost no correlation for the hemisphere + cylinder case. The dark blue regions in the wake of mode 3 are similar in shape to the blue regions in the mode 2 wake, especially for the hemisphere + cylinder case, but they are shifted in the streamwise direction. Combined with having similar modal spectra, as will be discussed later in this section, this indicates the presence of the traveling vortical structures along the edge of the separated region, which is consistent with the streamline pattern in Fig. 5. Mode 4 for these geometries is cross-stream antisymmetric and shows a strong anticorrelation in the wake similar to mode 1. This mode is also related to the alternating vortex shedding off of the turret and was observed in Ref. [12].

Different behavior is noticed in the POD modes for the partial hemisphere geometry, shown in the bottom row of Fig. 6, as compared to the hemisphere and hemisphere + cylinder geometries. Mode 1 for the partial hemisphere geometry contains 9% of the total energy and is symmetric with two highly correlated regions in the wake, which correspond to the reattachment region. Mode 2 for the partial hemisphere, which contains 6% of the energy, is cross-stream symmetric and primarily related to the vortices in the wake. This mode is similar to mode 1 but appears to be shifted in the streamwise direction, with the blue region located upstream of the similar blue region for mode 1. Downstream of the blue region, mode 2 has a cross-stream-symmetric region in yellow, which is anticorrelated with the blue region in the wake. As previously mentioned, the

similarity (up to a shift in the streamwise direction) of modes 1 and 2 indicates that these modes in fact represent a cross-stream-symmetric structure convecting downstream. For the partial hemisphere, the most dominant modes show almost no correlation between the wake and separation. This is a prominent departure from the flow dynamics observed for the hemisphere and the hemisphere + cylinder cases where there was a strong correlation between the separation line and the wake region for the first two modes, as seen in the middle and bottom rows of Fig. 6. So, it appears as though the separation line grows less influential as the protrusion decreases below the hemisphere. Modes 3 and 4 for the partial hemisphere case are primarily related to the structures in the wake, with only a small yellow region related to the separation line on top of the turret. These modes have a “checkerboard” pattern of the alternating blue and yellow regions in the wake. Similar to modes 1 and 2, these two modes also form a pair, with the spatially and primarily cross-stream antisymmetric shifted pattern. These modes appear to relate to alternating traveling vortices shed from opposite sides of the turret.

To further study the temporal dynamics of the dominant vortical structures in the pressure field, spectra of the time coefficients for the first four modes of each turret geometry were calculated using a Hanning window and block averaged over 16 blocks. The results are plotted in Fig. 8 as a function of the Strouhal number, $St_D = fD/U_\infty$, which is a normalized frequency based on the turret diameter.

The spectrum for mode 1 for the hemisphere + cylinder case, presented in the top-left plot of Fig. 8, shows a peak around $St_D \approx 0.19$. Similarly, the spectrum for mode 4 for the hemisphere + cylinder case has a clear peak at $St_D \approx 0.2$. The spectra for modes 2 and 3 do not have any prominent peaks, but they are similar, further indicating that modes 2 and 3 represent a traveling structure.

For the hemisphere case, spectra are shown in the top-right plot of Fig. 8. The cross-stream antisymmetric spectra for modes 1 and 4, plotted with a solid blue line and a dashed-dotted black line, also

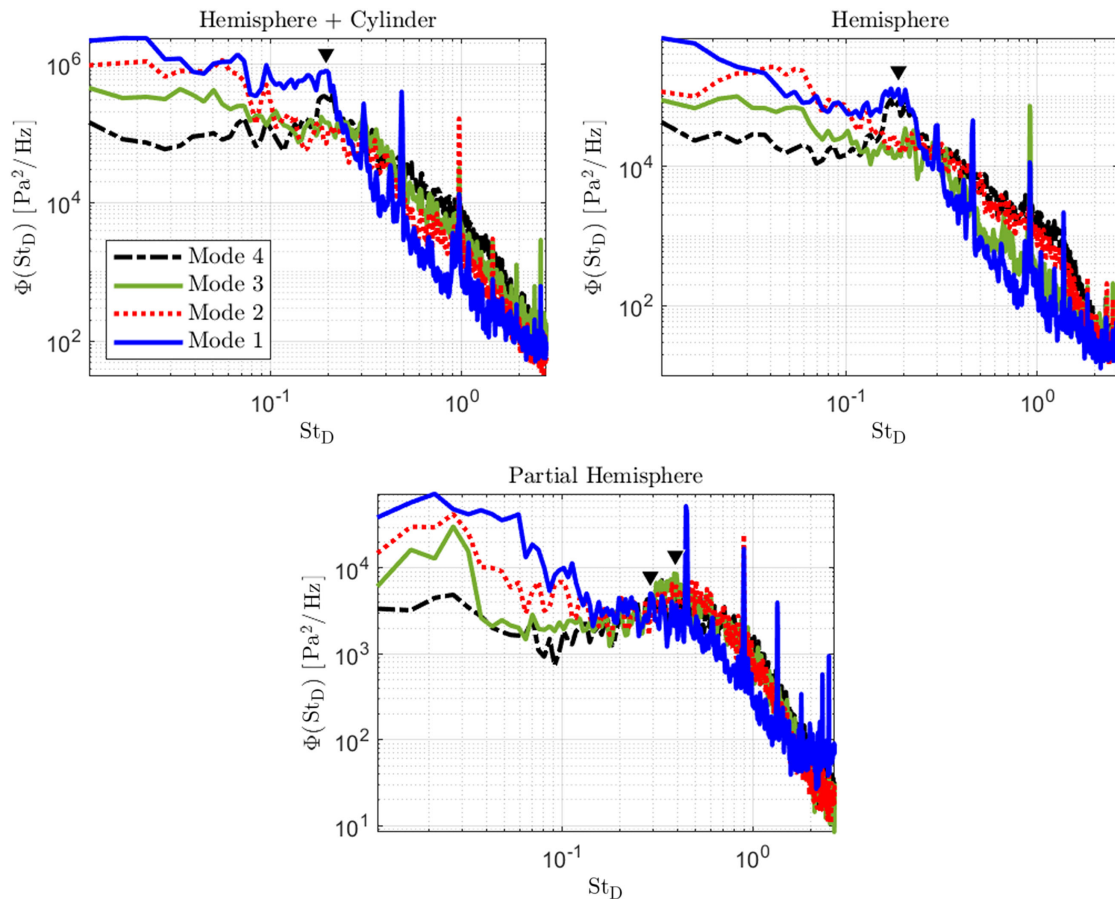


Fig. 8 Spectra of time coefficients for POD modes 1–4 for each geometry. Black inverted triangles denote significant peaks discussed in analysis.

have noticeable peaks at $St_D \approx 0.19$, respectively. This is consistent with results obtained in Refs. [10,12] and is associated with antisymmetric vortex shedding. This peak is more pronounced as compared to the hemisphere + cylinder case. Similar to the hemisphere + cylinder case, the spectra of modes 2 and 3 for the hemisphere case, plotted as dotted red and solid green lines, respectively, do not have any noticeable peaks. They do, however, have similar spectral shapes, indicating that modes 2 and 3 represent a traveling structure.

For the partial hemisphere case, shown in the bottom plot of Fig. 8, mode 1 has high energy in the lower frequencies below $St_D < 0.1$ with a slight broadband peak at $St_D \approx 0.3$. However, spectra for modes 2, 3, and 4 have a clear broadband peak that is most energetic at $St_D \approx 0.45$. This broadband peak is associated with symmetric vortex shedding [45]. From Fig. 8, it can be seen that although the hemisphere and hemisphere + cylinder cases have similar spectral characteristics, the modal spectra for the partial hemisphere are fundamentally different, further supporting the analysis based on the results presented in Figs. 6 and 7. However, one commonality between all modes and turret geometries is that the lower frequencies ($St_D < 0.5$) contain most of the spectral energy. Before moving on, it is also worth pointing out that sharp (narrowband) peaks appear in all of the spectra at around 160 Hz, 255 Hz, and subharmonics of 255 Hz ($St_D \approx 0.28, 0.47, 0.94$, etc.). These peaks were also observed in turret accelerometer data (not presented in this paper), indicating that these narrow peaks are associated with vibrations, and are not related to the flow features.

D. Joint POD Analysis

Although we gained some insight into the effects of different protrusions on the wake dynamics via POD analysis, the spatial regions for each turret geometry were different, making it difficult to compare POD modes between the geometries. As discussed in Sec. III.D, JPOD allows for a more direct comparison of the prominent flow features between different geometries by computing modes over the same region. As a reminder, JPOD finds spatial modes that are common (joint) for all geometries but have different amounts of energy, depending on the geometry. The first five JPOD modes are shown in Fig. 9. These modes are very similar to the POD modes of the hemisphere and the hemisphere + cylinder cases (see Fig. 6, middle and bottom rows) and follow the same interpretation. POD

mode 5 was not shown before; however, for the hemisphere and hemisphere + cylinder cases, it was also similar to JPOD mode 5 in Fig. 9. This mode is related to the breathing mode that has a pair of cross-stream-symmetric correlated structures in the wake (colored yellow) that are anticorrelated with another pair of structures downstream (shown in blue) and anticorrelated to the separation line region on top of the dome (also blue).

Individual relative modal energies for the first 10 JPOD modes are shown in the left-side plot of Fig. 10. The energy contribution for these JPOD modes is clearly different for the partial hemisphere as compared to the hemisphere and the hemisphere + cylinder cases. The most striking difference is that the most energetic mode for the partial hemisphere is cross-stream symmetric JPOD mode 1, whereas the most energetic JPOD mode for the hemisphere and the hemisphere + cylinders is cross-stream antisymmetric JPOD mode 2.

JPOD mode 1, associated with the symmetric wake breathing mode, is prominent for all three geometries. This mode was the most energetic for the partial hemisphere (18%), the second most energetic for the hemisphere + cylinder with 14% of the energy, and the third most energetic mode for the hemisphere with 9%. This leads to the conclusion that the wake breathing mode is a significant flow feature for all geometries.

JPOD mode 2 associated with the wake shifting mode contained 13 and 17% of the energy for the hemisphere and the hemisphere + cylinder, respectively. However, for the partial hemisphere, this mode had a small influence and only contained about 2% of the energy.

JPOD mode 3 is cross-stream symmetric with anticorrelation between the separation region on top of the turret and the wake region. This mode is the second-most energetic mode for the hemisphere, with 10% of the total energy. The mode is the third-most energetic for the hemisphere + cylinder, containing 13%. For the partial hemisphere, this mode was the second-most energetic but has a lower relative energy of 6%, indicating a lower correlation between the separation line and the wake regions.

So, between the full hemisphere and the partial hemisphere, the antisymmetric separation becomes much less prominent, and with decreased protrusion fluctuation of the separation region on top of the turret becomes less coherent. As a consequence, JPOD modes 1 and 2, which are nonzero on top of the turret, also decrease in relative strength.

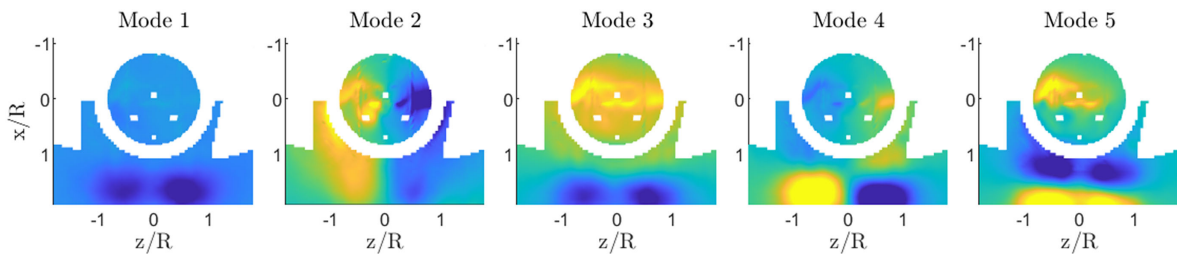


Fig. 9 First five JPOD modes. Flow goes from top to bottom.

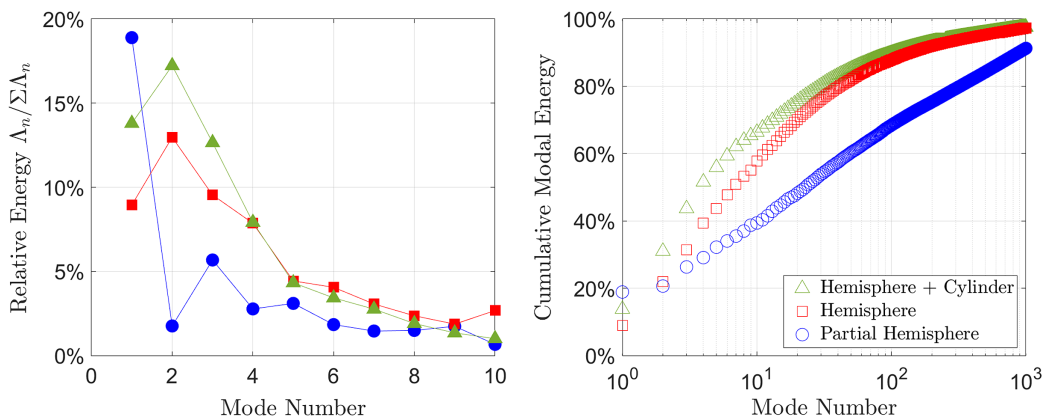


Fig. 10 Relative energy (left) and cumulative energy (right) of JPOD modes for each geometry.

JPOD mode 4 is a cross-stream-antisymmetric mode associated with the wake shifting and is primarily present in the hemisphere and the hemisphere + cylinder cases. JPOD mode 5 is a mostly cross-stream-symmetric mode and appears to be a spatially shifted version of JPOD mode 3. This mode has relatively low energy for all of the geometries, with less than 5% of the total energy for each geometry.

The relative cumulative energy for each geometry is shown in Fig. 10 (right-side plot). The hemisphere + cylinder case requires the least number of modes (around 110) to capture 90% of the total energy. The hemisphere case requires about 150 modes to reach the same relative energy, whereas the partial hemisphere requires a significantly higher number of modes (around 900). This suggests that the flow around the partial hemisphere is more complex and cannot be efficiently represented by a few dominant flow structures. We expect the flow dynamics to approach that of a flat plate boundary layer as the turret protrusion decreases, where the energy would be distributed across a wide range of scales and structures, making it more difficult to capture with a limited number of POD modes.

The spectra of the time coefficients for the first three JPOD modes of each geometry were calculated. The spectra were normalized by the total energy for a given mode Λ_n and are plotted in Fig. 11 versus the Strouhal number St_D . The normalized spectra for the hemisphere and the hemisphere + cylinder cases collapsed very well for JPOD modes 1–3. For cross-stream-symmetric JPOD mode 1, which corresponds to the strong correlation in the wake, the hemisphere and the hemisphere + cylinder cases have higher spectral energy at lower frequencies, with a peak at $St_D \approx 0.3$, and drop off for higher frequencies. The partial hemisphere has lower spectral energy as compared to the other two geometries in the lower frequencies with a peak around $St_D \approx 0.4$, and then it drops off for higher frequencies.

For antisymmetric JPOD mode 2, the spectra of the hemisphere and hemisphere + cylinder look similar to the spectra of their POD mode 1, shown in Fig. 8. This is an expected result because JPOD mode 2 and POD mode 1 look very similar. Both modes have a spectral peak at $St_D \approx 0.19$ that, again, is associated with the asymmetric vortex shedding. The hemisphere + cylinder case has a more pronounced peak with less spectral energy in the lower frequencies below $St_D \approx 0.19$ than the spectra of its POD mode 1. For the partial hemisphere case, the spectral peak in JPOD mode 2 is at a higher frequency than the other geometry's peaks at $St_D \approx 0.4$, with its lower frequencies having lower energy and its higher frequencies having higher energy. Overall, the energy of this mode is distributed more evenly across different frequencies than it is for the other geometries.

For cross-stream-symmetric JPOD mode 3 corresponding to the separation–wake relationship, the hemisphere and the hemisphere + cylinder cases both have higher spectral energy for the lower frequencies, which decreases for higher frequencies with no prominent peaks. For the partial hemisphere, however, the corresponding spectrum has lower spectral energy for the lower frequencies and has a small peak around $St_D \approx 0.5$; then, it drops off for higher frequencies.

Although not presented here, when plotted without normalization, it was found that the modal spectra for the partial hemisphere align well with that of the hemisphere for high frequencies of $St_D > 0.5$, but the partial hemisphere spectra contain significantly lower energy at $St_D < 0.5$ as compared to the hemisphere. This suggests that the lower-frequency fluctuations grow as protrusion increases from the partial hemisphere to the hemisphere, whereas the higher frequency fluctuations are relatively constant.

As a final comment, the computational work done by Malkus et al. [25] for a transonic case found that the spectra for the breathing

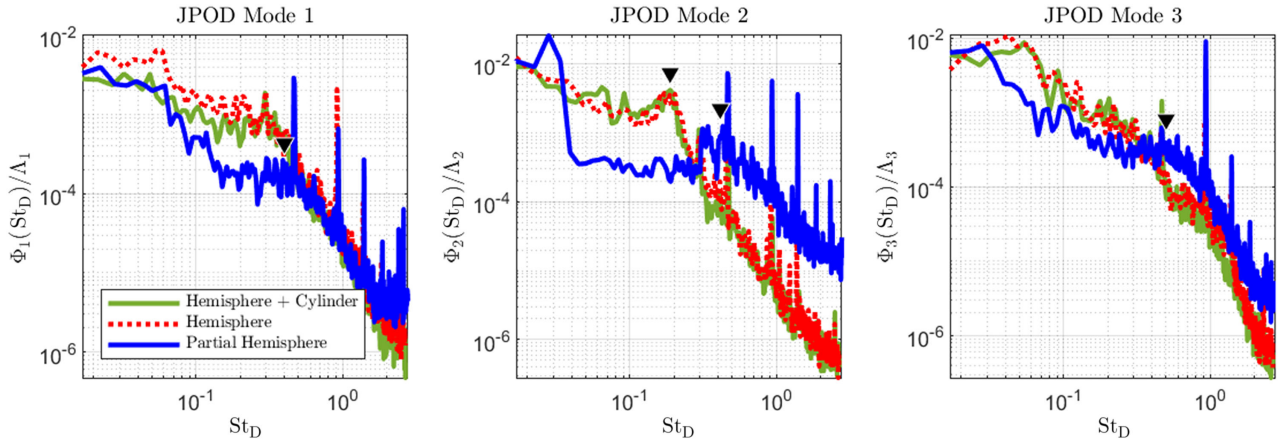


Fig. 11 Spectra for dominant JPOD modes for different geometries. Black inverted triangles denote significant peaks discussed in analysis.

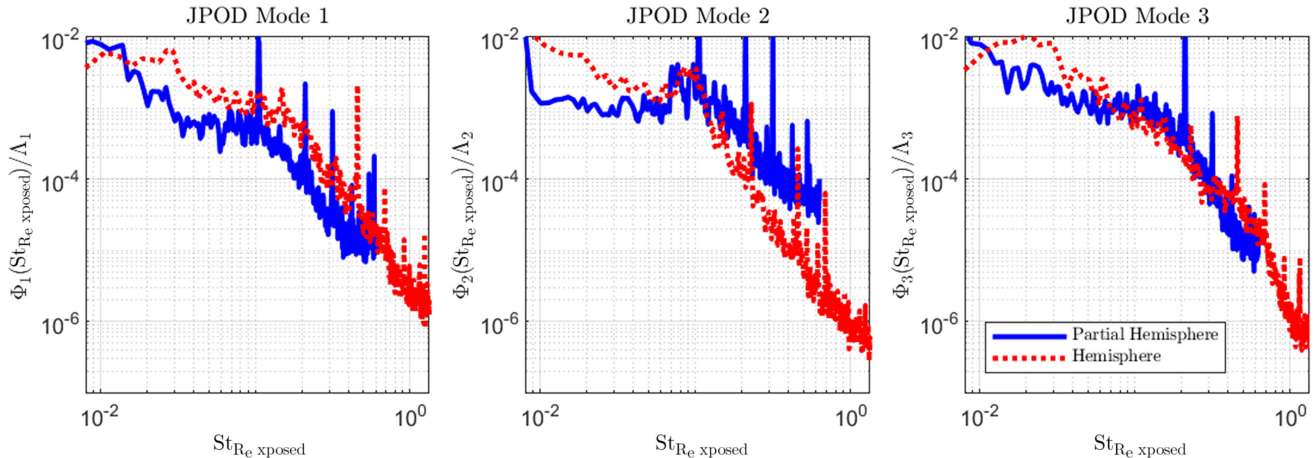


Fig. 12 Spectra for JPOD modes for different geometries, normalized by modal energy using $St_{Re,exposed}$, where $R_{exposed}$ is the radius of the dome of the turret that is protruded above the wall.

cross-stream-symmetric wake mode for both the hemisphere and the partial hemisphere cases shared a peak at a frequency of $St_D \approx 0.26$. Also, the spectrum for the shifting cross-stream antisymmetric mode has a peak between St_L of 0.13 and 0.21 if the reference length L in the definition of the Strouhal number is chosen to be the base diameter of the exposed turret. Because the partial hemisphere has a smaller base, the Strouhal number at the spectra peak will decrease with this scaling. However, when applied to the data in this analysis, this scaling did not have much effect; the spectra look similar to Fig. 11, and the peaks for the partial hemisphere and the hemisphere cases did not match. Reference [46] suggested using the distance from the wall to the top of the turret as the length scale in an attempt to collapse the spectra. This scaling was also tried as shown in Fig. 12. Although the peaks for JPOD mode 2 are aligned for the partial hemisphere and hemisphere, the spectra for the rest of the JPOD modes do not align well. The hemisphere + cylinder was not included in this comparison because Ref. [46] did not include hemisphere-on-cylinder data either, and using the diameter as the length scale has been shown to be a clear scaling between the hemisphere and the hemisphere + cylinder.

V. Conclusions

In the presented work, the unsteady surface pressure fields were measured on and in the wake region of hemisphere-on-cylinder turrets, with realistic surface features for different protrusions in Mach 0.5 flow using a fast-response pressure-sensitive paint. The tested geometries were a partial hemisphere with 45% of protrusion, a full hemisphere, and a hemisphere + cylinder. Unsteady pressure fields were used to compute velocity fields, associated with the convective vortical structures in the wake of the turret, using an optical flow approach. The resulting velocity fields were used to study the topology of the flow in the wake region, including identifying and characterizing different topological features of the wake. It was found that the separation region in the wake becomes thinner as the turret protrusion decreases, although the aspect ratio of the separation region was found to be relatively constant.

The unsteady pressure fields were also used to perform POD and joint POD modal analyses for these tested geometries to investigate the spatial distribution and spectra of different modes. For the geometries of greater protrusion (the hemisphere and the hemisphere + cylinder), the main dynamic wake mode was found to be a cross-stream-antisymmetric mode with a dominant spectral peak at $St_D \approx 0.19$. This mode was associated with the wake shifting mode, which was dominated by antisymmetric shedding of the vortices off the sides of the turret. This antisymmetric mode revealed a correlation between the separated region in the wake and the separation line on top of the turret; these results were consistent with other investigations.

However, when the protrusion was reduced to a partial hemisphere, a mode switching was observed where a primary wake mode became cross-stream symmetric, with a broadband peak at a higher frequency of $St_D \approx 0.3$. This mode was related to the wake breathing mode. It was also found that the surface pressure field of the partial hemisphere was overall less organized as compared to the other configurations. The organization that was present in the flow for the partial hemisphere resulted from the breathing mode, which was mostly active in the separation region of the wake, without much correlation with pressure fluctuations of the separation line. The breathing mode was also present for the hemisphere and hemisphere + cylinder cases, but it had a stronger correlation to the separation line as compared to the partial hemisphere case.

The analysis of the spectra of joint POD modes revealed that the spectra for the hemisphere and hemisphere + cylinder geometries had similar shapes when normalized by their relative energies. In contrast, the spectra of the JPOD modes for the partial hemisphere were quite different. Compared to the more protruding geometries, the spectra contained less energy at low frequencies below $St_D \approx 0.3$ – 0.45 , even when the breathing mode was significant for all the geometries. In an attempt to collapse the modal spectra for the partial hemisphere, length scales other than the turret diameter were used to normalize the frequency; however, none were able to collapse the

spectra for the partial hemisphere and the hemisphere. The presented modal analysis offers insight into the spatial and temporal dynamics of the pressure field on and around the turret at different protrusions. It also can be useful for validating computational codes for flow over turret geometries.

Acknowledgments

This work is supported by the U.S. Air Force Research Laboratory under cooperative agreement number FA9451-17-2-0088. The views expressed are those of the authors and do not necessarily reflect the official policy or position of the department of the U.S. Air Force, the U.S. Department of Defense, or the U.S. Government.

References

- [1] Gordeyev, S., and Jumper, E., "Fluid Dynamics and Aero-Optics of Turrets," *Progress in Aerospace Sciences*, Vol. 46, No. 8, 2010, pp. 388–400.
<https://doi.org/10.1016/j.paerosci.2010.06.001>
- [2] Kyrakis, D. T., "Airborne Laser Laboratory Departure from Kirtland Air Force Base and a Brief History of Aero-Optics," *Optical Engineering*, Vol. 52, No. 7, 2012, Paper 071403.
<https://doi.org/10.1117/1.OE.52.7.071403>
- [3] Ross, C. L., "Origins of the Airborne Laser," *Air Power History*, Vol. 58, No. 1, 2011, pp. 4–13.
- [4] Gordeyev, S., Post, M. L., McLaughlin, T., Cenicerros, J., and Jumper, E. J., "Aero-Optical Environment Around a Conformal-Window Turret," *AIAA Journal*, Vol. 45, No. 7, 2007, pp. 1514–1524.
<https://doi.org/10.2514/1.26380>
- [5] De Lucca, N. G., Gordeyev, S., and Jumper, E., "The Study of Aero-Optical and Mechanical Jitter for Flat Window Turrets," *50th AIAA Aerospace Sciences Meeting Including the New Horizons Forum and Aerospace Exposition*, AIAA Paper 2012-0623, 2012.
<https://doi.org/10.2514/6.2012-623>
- [6] Gordeyev, S., Jumper, E. J., and Whiteley, M., *Aero-Optical Effects: Physics, Analysis and Mitigation*, Wiley, Hoboken, NJ, 2023, pp. 152–179.
- [7] Kalensky, M., Kemnetz, M. R., and Spencer, M. F., "Effects of Shock Waves on Shack–Hartmann Wavefront Sensor Data," *AIAA Journal*, Vol. 61, No. 6, 2023, pp. 2356–2368.
<https://doi.org/10.2514/1.j062783>
- [8] Kalensky, M., Jumper, E. J., Kemnetz, M. R., and Gordeyev, S., "In-Flight Measurement of Atmospheric-Imposed Tilt: Experimental Results and Analysis," *Applied Optics*, Vol. 61, No. 16, 2022, Paper 4874.
<https://doi.org/10.1364/AO.460717>
- [9] Kalensky, M., "Airborne Measurement of Atmospheric-Induced Beam Jitter," Ph.D. Thesis, Univ. of Notre Dame, Notre Dame, IN, 2022.
- [10] Gordeyev, S., De Lucca, N., Jumper, E., Hird, K., Juliano, T., Gregory, J., Thordahl, J., and Wittich, D., "Comparison of Unsteady Pressure Fields on Turrets with Different Surface Features Using Pressure-Sensitive Paint," *Experiments in Fluids*, Vol. 55, No. 1, 2014, pp. 1–20.
<https://doi.org/10.1007/s00348-013-1661-9>
- [11] Hayashi, T., and Sakaue, H., "Dynamic and Steady Characteristics of Polymer-Ceramic Pressure-Sensitive Paint with Variation in Layer Thickness," *Sensors*, Vol. 17, No. 5, 2017, Paper 1125.
<https://doi.org/10.3390/s17051125>
- [12] De Lucca, N. G., Gordeyev, S., Morrida, J. J., Jumper, E. J., and Wittich, D. J., "Modal Analysis of the Surface Pressure Field Around a Hemispherical Turret Using Pressure Sensitive Paint," *2018 AIAA Aerospace Sciences Meeting*, AIAA Paper 2018-0932, Jan. 2018.
<https://doi.org/10.2514/6.2018-0932>
- [13] Gordeyev, S., Lucca, N. G. D., Morrida, J. J., and Jumper, E. J., "Conditional Studies of the Wake Dynamics of Hemispherical Turret Using PSP," *2018 AIAA Aerospace Sciences Meeting*, AIAA Paper 2018-2048, Jan. 2018.
<https://doi.org/10.2514/6.2018-2048>
- [14] De Lucca, N. G., Gordeyev, S., Jumper, E. J., Hird, K., Juliano, T. J., Gregory, J., Thordahl, J., and Wittich, D. J., "The Estimation of the Unsteady Aerodynamic Force Applied to a Turret in Flight," *44th AIAA Plasmadynamics and Lasers Conference*, AIAA Paper 2013-3136, June 2013.
<https://doi.org/10.2514/6.2013-3136>
- [15] Roeder, A. L., and Gordeyev, S., "Wake Response Downstream of a Spanwise-Oscillating Hemispherical Turret," *Journal of Fluids and Structures*, Vol. 109, Feb. 2022, Paper 103470.
<https://doi.org/10.1016/j.jfluidstructs.2021.103470>

- [16] Tavakol, M. M., Yaghoubi, M., and Motlagh, M. M., "Air Flow Aerodynamic on a Wall-Mounted Hemisphere for Various Turbulent Boundary Layers," *Experimental Thermal and Fluid Science*, Vol. 34, No. 5, 2010, pp. 538–553.
<https://doi.org/10.1016/j.exthermflusci.2009.11.007>
- [17] Savory, E., and Toy, N., "Hemisphere and Hemisphere-Cylinders in Turbulent Boundary Layers," *Journal of Wind Engineering and Industrial Aerodynamics*, Vol. 23, Jan. 1986, pp. 345–364.
[https://doi.org/10.1016/0167-6105\(86\)90054-1](https://doi.org/10.1016/0167-6105(86)90054-1)
- [18] Morgan, P., and Visbal, M., "Effectiveness of Flow Control over a Submerged Hemispherical Flat-Window Turret," *51st AIAA Aerospace Sciences Meeting Including the New Horizons Forum and Aerospace Exposition*, AIAA Paper 2013-1015, 2013.
<https://doi.org/10.2514/6.2013-1015>
- [19] Jelic, R., Sherer, S., and Greendyke, R., "Simulation of Various Turrets at Subsonic and Transonic Flight Conditions Using Overflow," *Journal of Aircraft*, Vol. 50, No. 2, 2013, pp. 398–409.
<https://doi.org/10.2514/1.C031844>
- [20] Coirier, W. J., Whiteley, M., Goorskey, D. J., Drye, R., Barber, J., Stutts, J., and Porter, C., "Aero-Optical Evaluation of Notional Turrets in Subsonic, Transonic and Supersonic Regimes," *45th AIAA Plasmadynamics and Lasers Conference*, AIAA Paper 2014-2355, June 2014.
<https://doi.org/10.2514/6.2014-2355>
- [21] Woszidlo, R., Taubert, L., and Wagnanski, I., "Manipulating the Flow over Spherical Protuberance in a Turbulent Boundary Layer," *AIAA Journal*, Vol. 47, No. 2, 2009, pp. 437–450.
<https://doi.org/10.2514/1.39930>
- [22] Kalensky, M., Catron, B., Gordeyev, S. V., Jumper, E. J., and Kemnetz, M., "Investigation of Aero-Mechanical Jitter on a Hemispherical Turret," *Unconventional Imaging and Adaptive Optics 2021*, edited by J. J. Dolne, and M. F. Spencer, Vol. 11836, International Soc. for Optics and Photonics, Bellingham, WA, 2021, Paper 1183606.
<https://doi.org/10.1117/12.2588232>
- [23] Kalensky, M., Catron, B., Gordeyev, S., Jumper, E. J., and Kemnetz, M., "Pressure Sensitive Paint Measurements on a Hemispherical Turret," *Unconventional Imaging and Adaptive Optics 2021*, edited by J. J. Dolne, and M. F. Spencer, Vol. 11836, International Soc. for Optics and Photonics, Bellingham, WA, 2021, Paper 1183607.
<https://doi.org/10.1117/12.2595385>
- [24] Bukowski, T. J., Kalensky, M., Gordeyev, S., and Kemnetz, M., "Modal Analysis of Pressure Fields on and Around Turrets with Different Protrusions," *Unconventional Imaging and Adaptive Optics 2022*, edited by J. J. Dolne, and M. F. Spencer, Vol. 12239, International Soc. for Optics and Photonics, Bellingham, WA, 2022, Paper 122390F.
<https://doi.org/10.1117/12.2633429>
- [25] Malkus, M. J., Frede, M. T., Sherer, S. E., and Garmann, D. J., "Effect of Submergence on Transonic Flow Around a Hemisphere," *AIAA Journal*, Vol. 60, No. 11, 2022, pp. 6082–6096.
<https://doi.org/10.2514/1.J061811>
- [26] Lucca, N. G. D., Gordeyev, S. V., and Jumper, E. J., "In-Flight Aero-Optics of Turrets," *Optical Engineering*, Vol. 52, No. 7, 2013, Paper 071405.
<https://doi.org/10.1117/1.OE.52.7.071405>
- [27] Jumper, E. J., Zenk, M. A., Gordeyev, S. V., Cavalieri, D. A., and Whitely, M., "Airborne Aero-Optics Laboratory," *Optical Engineering*, Vol. 52, No. 7, 2013, pp. 1–12.
<https://doi.org/10.1117/1.OE.52.7.071408>
- [28] Morrida, J., Gordeyev, S., Lucca, N. D., and Jumper, E. J., "Shock-Related Effects on Aero-Optical Environment for Hemisphere-On-Cylinder Turrets at Transonic Speeds," *Applied Optics*, Vol. 56, No. 16, 2017, pp. 4814–4824.
<https://doi.org/10.1364/AO.56.004814>
- [29] De Lucca, N. G., Gordeyev, S., Morrida, J. J., and Jumper, E. J., "Investigation of Flow Dynamics over Turrets with Different Spanwise Aspect Ratios Using PSP," *2018 AIAA Aerospace Sciences Meeting*, AIAA Paper 2018-2047, Jan. 2018.
<https://doi.org/10.2514/6.2018-2047>
- [30] Gray, P. D., Gluzman, I., Thomas, F., Corke, T., Lakebrink, M., and Mejia, K., "A New Validation Experiment for Smooth-Body Separation," *AIAA Aviation 2021 Forum*, AIAA Paper 2021-2810, Aug. 2021.
<https://doi.org/10.2514/6.2021-2810>
- [31] Porter, C., Gordeyev, S., Zenk, M., and Jumper, E., "Flight Measurements of the Aero-Optical Environment Around a Flat-Windowed Turret," *AIAA Journal*, Vol. 51, No. 6, 2013, pp. 1394–1403.
<https://doi.org/10.2514/1.J052067>
- [32] Sakaue, H., Kakisako, T., and Ishikawa, H., "Characterization and Optimization of Polymer-Ceramic Pressure-Sensitive Paint by Controlling Polymer Content," *Sensors*, Vol. 11, No. 7, 2011, pp. 6967–6977.
<https://doi.org/10.3390/s110706967>
- [33] Hayashi, T., and Sakaue, H., "Temperature Effects on Polymer-Ceramic Pressure-Sensitive Paint as a Luminescent Pressure Sensor," *Aerospace*, Vol. 7, No. 6, 2020, Paper 80.
<https://doi.org/10.3390/aerospace7060080>
- [34] Carlbom, I., and Paciorek, J., "Planar Geometric Projections and Viewing Transformations," *ACM Computing Surveys*, Vol. 10, No. 4, 1978, pp. 465–502.
<https://doi.org/10.1145/356744.356750>
- [35] Haralick, R. M., "Using Perspective Transformations in Scene Analysis," *Computer Graphics and Image Processing*, Vol. 13, No. 3, 1980, pp. 191–221.
[https://doi.org/10.1016/0146-664X\(80\)90046-5](https://doi.org/10.1016/0146-664X(80)90046-5)
- [36] Tan, T. N., Sullivan, G. D., and Baker, K. D., "On Computing the Perspective Transformation Matrix and Camera Parameters," *Proceedings of the British Machine Vision Conference*, edited by J. Illingworth, BMVA Press, Durham, England, U.K., 1993, pp. 13.1–13.10.
<https://doi.org/10.5244/C.7.13>
- [37] Lucas, B. D., and Kanade, T., "An Iterative Image Registration Technique with an Application to Stereo Vision," *Proceedings of the 7th International Joint Conference on Artificial Intelligence*, Vol. 2, Aug. 1981, pp. 674–679.
- [38] Lee, T., Lee, C., Nonomura, T., and Asai, K., "Unsteady Skin-Friction Field Estimation Based on Global Luminescent Oil-Film Image Analysis," *Journal of Visualization*, Vol. 23, Oct. 2020, pp. 763–772.
<https://doi.org/10.1007/s12650-020-00661-y>
- [39] Lee, T., Nonomura, T., Asai, K., and Liu, T., "Linear Least-Squares Method for Global Luminescent Oil Film Skin Friction Field Analysis," *Review of Scientific Instruments*, Vol. 89, No. 6, 2018, Paper 065106.
<https://doi.org/10.1063/1.5001388>
- [40] Taira, K., Brunton, S. L., Dawson, S. T. M., Rowley, C. W., Colonius, T., McKeon, B. J., Schmidt, O. T., Gordeyev, S., Theofilis, V., and Ukeiley, L. S., "Modal Analysis of Fluid Flows: An Overview," *AIAA Journal*, Vol. 55, No. 12, 2017, pp. 4013–4041.
<https://doi.org/10.2514/1.J056060>
- [41] Gordeyev, S., and Thomas, F. O., "Coherent Structure in the Turbulent Planar Jet. Part 1. Extraction of Proper Orthogonal Decomposition Eigenmodes and their Self-Similarity," *Journal of Fluid Mechanics*, Vol. 414, July 2000, pp. 145–194.
<https://doi.org/10.1017/S002211200000848X>
- [42] Gordeyev, S., Vorobiev, A., Jumper, E. J., Gogineni, S. P., and Wittich, D. J., "Studies of Flow Topology around Hemisphere at Transonic Speeds Using Time-Resolved Oil Flow Visualization," *54th AIAA Aerospace Sciences Meeting*, AIAA Paper 2016-1459, Jan. 2016.
<https://doi.org/10.2514/6.2016-1459>
- [43] Kalensky, M., Gordeyev, S., and Jumper, E. J., "In-Flight Studies of Aero-Optical Distortions Around AAOL-BC," *AIAA Aviation 2019 Forum*, AIAA Paper 2019-3253, June 2019.
<https://doi.org/10.2514/6.2019-3253>
- [44] De Lucca, N. G., "Studies of the Pressure Field and Related Beam Jitter for Hemisphere-on-Cylinder Turrets," Ph.D. Thesis, Univ. of Notre Dame, Notre Dame, IN, 2016.
- [45] Manhart, M., "Vortex Shedding from a Hemisphere in a Turbulent Boundary Layer," *Theoretical and Computational Fluid Dynamics*, Vol. 12, No. 1, 1998, pp. 1–28.
<https://doi.org/10.1007/s001620050096>
- [46] Palavicini, M., Cattafesta, L., and George, B., "Passive Flow Control over a Three-Dimensional Turret with a Flat Aperture," *41st AIAA Fluid Dynamics Conference and Exhibit*, AIAA Paper 2011-3265, June 2011.
<https://doi.org/10.2514/6.2011-3265>

Y. Zhou
Associate Editor